HHS Public Access

Author manuscript

IEEE Trans Biomed Eng. Author manuscript; available in PMC 2022 May 01.

Published in final edited form as:

IEEE Trans Biomed Eng. 2021 May ; 68(5): 1536–1546. doi:10.1109/TBME.2020.3036535.

Rapid impedance spectroscopy for monitoring tissue impedance, temperature, and treatment outcome during electroporation-based therapies

Melvin F. Lorenzo [Graduate Student Member, IEEE],
Department of Biomedical Engineering and Mechanics, Virginia Tech, Blacksburg, VA, 24061 USA.

Suyashree P. Bhonsle [Member, IEEE],
Department of Electrical and Computer Engineering, Virginia Tech, Blacksburg, VA, 24061 USA.

Christopher B. Arena [Member, IEEE],
Department of Biomedical Engineering and Mechanics, Virginia Tech, Blacksburg, VA, 24061 USA.

VoltMed Inc., Blacksburg, VA, 24061 USA

Rafael V. Davalos [Member, IEEE]
Department of Biomedical Engineering and Mechanics, Virginia Tech, Blacksburg, VA, 24061 USA.

Abstract

Objective: Electroporation-based therapies (EBTs) employ high voltage pulsed electric fields (PEFs) to permeabilize tumor tissue; this results in changes in electrical properties detectable using electrical impedance spectroscopy (EIS). Currently, commercial potentiostats for EIS are limited by impedance spectrum acquisition time (~10s); this timeframe is much larger than pulse periods used with EBTs (~1s). In this study, we utilize rapid EIS techniques to develop a methodology for characterizing electroporation (EP) and thermal effects associated with high-frequency irreversible EP (H-FIRE) in real-time by monitoring inter-burst impedance changes.

Methods: A charge-balanced, bipolar rectangular chirp signal is proposed for rapid EIS. Validation of rapid EIS measurements against a commercial potentiostat was conducted in potato tissue using flat-plate electrodes and thereafter for the measurement of impedance changes throughout IRE treatment. Flat-plate electrodes were then utilized to uniformly heat potato tissue; throughout high-voltage H-FIRE treatment, low-voltage inter-burst impedance measurements were used to continually monitor impedance change and to identify a frequency at which thermal effects are delineated from EP effects.

Corresponding author: Christoper B. Arena. carena@vt.edu.

Results: Inter-burst impedance measurements (1.8 kHz – 4.93 MHz) were accomplished at 216 discrete frequencies. Impedance measurements at frequencies above ~1 MHz served to delineate thermal and EP effects in measured impedance.

Conclusion: We demonstrate rapid-capture (<<1s) EIS which enables monitoring of inter-burst impedance in real-time. For the first time, we show impedance analysis at high frequencies can delineate thermal effects from EP effects in measured impedance.

Significance: The proposed waveform demonstrates the potential to perform inter-burst EIS using PEFs compatible with existing pulse generator topologies.

Index Terms—

Electropermeabilization; electrical impedance spectroscopy; irreversible electroporation; bipolar pulses

I. Introduction

Treatment options for nonresectable tumors are restricted due to multiple clinical factors, notably because of their proximity to critical structures (large blood vessels and nerve bundles). Alternate thermal therapies like microwave ablation, radiofrequency ablation, and cryoablation are also limited by tumor location as they can cause indiscriminate damage [1]. Thus, EBTs are appealing and have proven advantageous for treating nonresectable tumors due to their nonthermal mechanisms of cell death, which preserve proteinaceous structures including nerves and vasculature [2], [3].

Clinically, EBTs are applied using an array of needle electrodes placed in and around the target tissue. High amplitude (up to 3000 V), short duration (50 – 100 μs) PEFs are applied across the electrodes, exposing tissues to high local electric fields. This results in an increased transmembrane potential and gives rise to the creation of defects on the cell membrane [4]. In a systematic review, electrochemotherapy (ECT), which utilizes reversible EP for enhanced drug delivery, demonstrates an increased overall complete response rate compared to drug therapy alone [5], [6]. Irreversible electroporation (IRE) demonstrates comparable efficacy [7]–[9].

Despite widespread use, EBTs face a unique challenge: real-time intraoperative monitoring of treatment progression. Current approaches to determine treatment outcome rely either on postoperative imaging with MRI and ultrasound techniques [10], [11] or perioperative electrical impedance measurements. In contrast to EBTs, thermal ablation modalities utilize intraoperative temperature measurements to predict treatment volumes in real-time [12]. Analogous to this approach, throughout PEF treatment, cell membrane permeabilization causes impedance changes due to decreased membrane resistance [13] and exchange of intra- and extra- cellular ionic content [14]. These impedance changes are the target for proposed methods of monitoring treatment progression.

Tissue impedance analysis, employed with bursts of bipolar PEFs, can be classified into two categories: 1) intra-burst impedance measurements (or in-pulse impedance [15], [16]), the impedance analysis of the high-voltage therapeutic PEFs, and 2) inter-burst impedance

measurements, the low-voltage impedance analysis at discrete timepoints between therapeutic PEFs. At low-voltages, the intact cell membrane restricts low-frequency electric currents to the extracellular domain; high frequency currents short the membrane reactance, allowing current flow through the cell (Fig. 1a). High-voltage PEFs compromise the cell membrane, allowing all currents to flow through the cell (Fig. 1a).

An application for intra-burst (in-pulse) impedance has focused on quantifying changes in tissue conductivity during the EBT pulse [16], aimed towards the creation of accurate pre-treatment planning models [17], [18]. Circuit model representations of biological cells, like that shown in Fig. 1b, can be used to quantify these effects as the change in conductivity due to EP is reflected as a decrease in membrane resistance [13]. As mentioned previously, inter-burst impedance measurements have been used to gauge extent of EP. Proposed solutions for monitoring EP progression include: 1) electrical impedance tomography (EIT) [19], [20], 2) electrical impedance spectroscopy (EIS) to measure impedance with a four-electrode method [15] or with an impedance sensing array [21], and 3) current density imaging with B_Z-based Magnetic Resonance EIT (MREIT) to predict cell kill [22]. While these technologies are successful in mapping tissue impedance changes following treatment, limitations include: difficulties integrating these technologies with existing pulse generators, the cost or expense associated with additional equipment, and the impedance spectrum acquisition timeframe (~10s) which is typically much larger than that between pulse periods (~1s) used with EBTs.

To this end, methods for rapid bioimpedance measurements have been proposed. In summary, rapid EIS measurements utilize low-voltage or low-current stimulus, subsequent Fourier Transform, followed by analysis in the frequency domain. Above all else, these methods should be performed to minimize inclusion of significant nonlinearities. In the case of EP, the signal amplitude should be restricted so as to avoid membrane electroporation [23]. Several stimulation signals have been proposed, including multisine waves [24], Gaussian pulses [25], maximum length binary sequences [26], rectangular chirps [27], and white-noise [28]. We bring attention to the works of Pliquette et al [29], [30], Ivorra et al. [15], [31], García-Sánchez et al [32], [33], and Bürgel et al [34] for applications in EP.

In this study, we utilize rapid EIS as a methodology for monitoring tissue inter-burst impedance changes during EBTs in real-time. Direct applications of this methodology are geared towards determining a clinical endpoint to EBTs, specifically with ablative IRE technologies, as well as delineating thermal effects from EP using tissue impedance measurements. To accomplish rapid EIS, a charge balanced, rectangular bipolar chirp signal is proposed and utilized for inter-burst impedance measurements. Previously, García-Sánchez et al. proposed utilization of a multi-sine burst for inter-burst impedance analysis between 5 kHz to 1.313 MHz at 21 discrete frequencies [32]. Preference to using rectangular PEFs, over sinusoidal excitation signals [35], is such that rectangular waveforms are easily integrated into existing pulse generator topologies as the pulse widths implemented are similar to those delivered with nanosecond PEFs [36], high-frequency bipolar PEFs [37]–[40], and monopolar PEFs [41], [42]. Therefore, implementation and translation of this technique in a clinical setting is readily achievable.

Previously, we utilized a Fourier analysis to quantify intra-burst impedance changes during H-FIRE therapy [16]. In this study, we extend our initial findings to develop a method for inter-burst EIS using custom waveforms compatible with existing EBT pulse generators. Our findings suggest acquisition of high-bandwidth inter-burst impedance spectra (1.8 kHz – 4.93 MHz) is possible at >100 discrete frequencies and at capture rates <<1s. This technique presents with applications for monitoring clinical endpoints of IRE technologies using real-time EIS. In addition, this technique allows for novel applications of high-frequency impedance measurements as a parameter to delineate thermal effects from that of EP throughout EBTs.

II. Methods

A. Nomenclature and Overview of Experimental Protocols

Firstly, we introduce nomenclature to define the burst scheme used for impedance measurements. Like that of high-frequency IRE, the burst scheme is constructed as: positive phase – intra-phase delay – negative phase – inter-pulse delay μs (Fig. 2). As the goal for the inter-burst EIS waveform is to attain impedance measurements at wide frequency bands, intuitively, this can be accomplished by means of a chirp signal. The inter-burst EIS waveform is composed of a high-frequency burst 1-50-1-50 μs (energized-time 164 μs) appended to a low-frequency burst 250-10-250-10 μs (energized-time 1 ms) for a combined signal duration 9.608 ms. For comparison to the inter-burst EIS waveform, an H-FIRE waveform of burst scheme 2-5-2-100 μs and energized-time 100 μs (signal duration 2.725 ms) is also tested. This H-FIRE burst scheme features an extended inter-pulse delay [39].

Validation of rapid EIS is accomplished using a vegetal tissue model (potato tuber tissue). Potato tissue has been previously used as an *in vitro* model for impedance spectroscopy techniques [43], [44].

Preliminary validation is accomplished by comparing inter-burst impedance against that of a commercial potentiostat Gamry Reference 600 (Gamry, Warminster, PA, US). A flat-plate electrode configuration is used to characterize impedance of intact potato tissue exposed to a uniform electric field. Next, we transition to a two-needle configuration to implement rapid EIS in a more clinically relevant electrode configuration. Rapid EIS is used to measure inter-burst/interpulse impedance throughout IRE treatment and is validated against the potentiostat. Finally, we postulate high-frequency impedance measurements can delineate thermal and EP effects from measured impedance changes during EBTs. As low-frequency impedance measurements are sensitive to both EP effects and Joule heating, we hypothesize that high-frequency impedance measurements, corresponding to electric currents which short the membrane reactance, are less sensitive to EP effects and can uniquely act to distinguish thermal effects (Fig. 1c). This hypothesis is examined by uniformly heating potato tissue using H-FIRE and analyzing inter-burst impedance measurements to continually monitor changes in tissue impedance and to identify the optimal frequency for thermal analysis.

B. Signal Processing in MATLAB for Impedance Extraction

In all cases presented, the experimentally recorded voltage waveforms V(t) and current waveforms I(t) were analyzed in MATLAB vR2018a (MathWorks Inc., Natick, MA, US) using the Fast Fourier Transform (FFT) algorithm. The length of the FFT was defined as the next power of 2 from the length of the voltage signal. This resulted in $V(f)$ and $I(f)$, thereafter the magnitude of $V(f)$, labeled as $|V_{FFT}|$, was defined. To identify and isolate high-power peaks in $|V_{FFT}|$, a peak extraction algorithm in MATLAB was implemented; a single data point was extracted from each high-power peak if the power of the peak was a threshold value 2% of max($|V_{FFT}|$). The data points identified were subsequently extracted from $V(f)$ and $I(f)$, where the impedance was calculated using:

$$Z(f) = \frac{V(f)}{I(f)} \quad (1)$$

MATLAB functions “real()” and “imag()” were used to analyze real and imaginary parts of the impedance, respectively. The sampling period of the recorded waveforms was 20 ns (50 MHz). Inter-burst EIS waveform contained 500,001 samples in the time domain.

C. Validation of rapid EIS Against a Commercial Potentiostat

Russet potato tissue was sliced to a thickness 0.7 cm and further sectioned using a cylindrical cutter of diameter 0.8 cm. This tissue sample was placed between two flat-plate electrodes with square cross section 2 × 2 cm (BTX, Harvard Apparatus, Cambridge, MA). A baseline impedance spectrum was measured using the potentiostat at a frequency band 1 kHz to 1 MHz at 10 points per decade. The potentiostat impedance spectrum served as a comparison to assess accuracy of rapid EIS. Following EIS with the commercial potentiostat, low-voltage inter-burst waveform and low-voltage H-FIRE was delivered using an AFG31000 function generator (Tektronix Inc., Beaverton, OR, US) at a voltage 15 V. The voltage and current waveforms were recorded using a WaveSurfer 3024z Oscilloscope (Teledyne LeCroy, Chestnut Ridge, New York) and a 1× current probe (2877, Pearson Electronics, Palo Alto, California). V(t) and I(t) were analyzed as mentioned previously. It should be mentioned, the intended rapid EIS waveform is the chirp signal, whereas the low-voltage H-FIRE waveform is presented merely as a direct comparison.

D. Monitoring Impedance Change and Ablation Outcome

Inter-burst/inter-pulse EIS was used to monitor tissue impedance changes and ablation outcomes following the application of IRE pulses in russet potato tissue. Potatoes were sectioned uniformly to a 0.7 cm thickness with an ellipsoidal cross section ~15×10 cm. Two, 20-gauge cylindrical stainless-steel needle electrodes were inserted at the center of the sample and maintained at a 1 cm spacing; these electrodes were used for both EIS and tissue ablation with IRE. Prior to tissue ablation, baseline impedance and inter-burst EIS were implemented as described in the previous section.

Following baseline impedance characterization, 1, 5, 10, 20, 40, and 80 IRE pulses were delivered at 1000 V and 100 μs on-time (n = 9); additional impedance measurements were taken following each pulse group. To mitigate thermal effects on the measured impedance

and to allow for impedance capture with the potentiostat, IRE pulses were delivered in sets of 10, where applicable, with a 1-minute delay in between each set. Potatoes were covered in plastic wrap and stored for 24 hrs to allow for tissue oxidation. The oxidized area served to quantify the ablative region and was measured in ImageJ software.

E. Delineating Temperature Effect from EP using High-Frequency Impedance Measurements

We hypothesize high-frequency impedance measurements are less susceptible EP effects and can therefore serve to delineate thermal impact from EP. To test this, we use a flat-plate electrode configuration to uniformly heat potato tissue.

A russet potato was sectioned to a rectangular shape factor of length, width, and thickness 2×2×0.7 cm. This tissue was placed between flat-plate electrodes. A prototype board was constructed to interlace inter-burst EIS and H-FIRE, set 500 ms apart, so as to monitor changes in inter-burst impedance (0.5 Hz) throughout treatment. The prototype board consisted of a custom high-voltage bipolar pulse generator [45] and a custom low-voltage bipolar pulse generator isolated using 4 individual Reed relays (5503-05-1, Coto Technology, Sunnyvale, California). The Reed relays, HV pulser, and LV pulser were synchronized using an Arduino Uno microcontroller (Arduino LLC, Boston, MA). Prior to treatment, baseline impedance (Z_0) was quantified. 300 bursts of H-FIRE (2-5-2-100 μs, 1,400 V, energized time of 40 μs per burst) were delivered across a rectangular tissue section. High-frequency noise was present in the prototype low-voltage pulser, therefore a 9th order low-pass filter with cutoff frequency 5 MHz was implemented and data above 3 MHz was excluded for analysis. During treatment, temperature was monitored at 30 Hz using a FLIR A325SC thermal camera (FLIR, Wilsonville, OR, USA) and the temperature profile defined as the average surface temperature over a 3×3 rectangular grid (9 points).

Temperature increase was quantified assuming temperature increases linearly with a fixed temperature coefficient of conductivity (equation (2)). A substitution was implemented to express this relationship in terms of the real part of the impedance: $\sigma = 1/(Z_{real} \cdot K)$, where K is the shape factor. Here, an assumption is made: in either an intact state or a state in which the cell membrane if compromised, the circuit model shown in Fig. 1b indicates the real part of the impedance reflects the resistive portion of the impedance measurements. This resolves in equation (3), where Z_N is the N^{th} burst impedance and Z_{N+1} is the subsequent burst impedance. In addition, an analysis is conducted to quantify temperature increase using the magnitude of the impedance, as opposed to the real part of the impedance, and this result is overlaid with that of the real part of the impedance. As changes in low-frequency impedance measurements are attributed to both EP and thermal effects, we use variable $\Delta\theta$ to represent increase in temperature across all frequencies.

$$\sigma = \sigma_0 \cdot (1 + \alpha \cdot \Delta T) \tag{2}$$

$$\Delta\theta(t) = \frac{Z_N - Z_{N+1}}{Z_{N+1}} \cdot \frac{1}{\alpha} \tag{3}$$

Here, α represents the temperature coefficient of conductivity (α = 3.0 %/°C was used [44]). It can be concluded that the frequency for which $\Delta\theta$ converges to ΔT represents a frequency at which EP effects are minimized. The $\Delta\theta$ profile and plots were developed for 1.8 kHz, 17.5 kHz, 181 kHz, 1.23 MHz, and 2.99 MHz. In addition, the maximum $\Delta\theta$ along the $\Delta\theta$ profile was quantified as a function of frequency.

F. Statistical analysis

Nonlinear regression analysis was performed and a null hypothesis describing "a single curve fit" between the commercial potentiostat and rapid EIS impedance data was tested. Here, a p-value < 0.05 was considered statistically significant (null hypothesis rejected). The R^2 reported are those relative to the global/shared curve fit between the potentiostat and rapid EIS impedance. The real part of the impedance for all data sets was fit to a 4-parameter logistic regression model, an adaptation to the Cole-equation:

$$Z_{\text{real}} = Z_{\infty} + \frac{Z_0 - Z_{\infty}}{1 + (f \cdot b)^c} \tag{4}$$

The measured ablations were compared using a one-way ANOVA with a post-hoc Tukey's multiple comparisons test. A p-value < 0.05 was considered statistically significant. Statistical analysis was conducted in GraphPad Prism v8.2.

III. Results

A. Rapid EIS Impedance is Comparable to a Potentiostat

Recorded low-voltage inter-burst EIS and H-FIRE are seen in Fig. 3a–b. The $|V_{FFT}|$ plot shows an abundance of high-power peaks along the desired frequency range (Fig. 3c–d); the minimum and maximum frequency at which data was extracted for inter-burst EIS were 1.8 kHz and 4.93 MHz, respectively, spanning 216 discrete frequencies. For LV H-FIRE, the minimum and maximum frequency for data acquisition were 18.3 kHz and 1.96 MHz, respectively, spanning 170 discrete frequencies.

Nonlinear regression was conducted to test a null hypothesis for a single curve fit being used to describe the potentiostat and inter-burst/H-FIRE datasets. For Z_{real} of the inter-burst and LV H-FIRE recordings, the null hypotheses were valid: p = 0.487 and p = 0.405, respectively. The coefficient of determination between the global fits and the rapid EIS Z_{real} data was R^2 = 0.995 for inter-burst and R^2 = 0.997 for LV H-FIRE recordings (Fig. 3e–f). In both cases, the null hypothesis for Z_{imag} was rejected, though R^2 was determined as 0.987 for inter-burst and 0.996 for LV H-FIRE recordings (Fig. 3g–h). The flat-plate electrode experiments demonstrated that standard laboratory equipment allows for reliable impedance measurements with the proposed rapid-EIS waveforms.

B. Rapid Inter-burst Impedance is Proficient in Monitoring Impedance Change and Ablation Outcome

Transitioning to a two needle-electrode configuration, Fig. 4a depicts the bulk Z_{real} acquired prior to IRE treatment. Differences between the measured potentiostat impedance were

minimal; a single curve fit between potentiostat and inter-burst impedance can be described ($p = 0.216$, $R^2 = 0.990$).

Thereafter, IRE was delivered at a pulsing rate 1 Hz; of the 6 treatment groups (Table I), pulses for groups 4 – 6 were split into sets of 10 and a 1 minute delay added in between sets to allow for impedance capture with the potentiostat (> 10 s) and rapid EIS (<< 1 s). All groups demonstrated an IRE ablation, with 1 pulse (1P) group showing the smallest ablation (1.63 ± 0.26 cm^2). As the number of pulses was increased, the ablation area increased: 5P (2.23 ± 0.34 cm^2), 10P (3.45 ± 0.49 cm^2), 20P (3.92 ± 0.33 cm^2), 40P (4.44 ± 0.35 cm^2), and lastly the 80P group resolving in the largest measured ablation (4.57 ± 0.29 cm^2) (Fig. 4d). A one-way ANOVA with Tukey's post hoc multiple comparisons test revealed statistical differences between all treatment groups except for the 10P vs 20P group ($p = 0.074$) and the 40P vs 80P groups ($p = 0.964$). After 20 pulses, there is a slowed progression in ablation size after additional pulses, with the 40P and 80P groups showing no statistical differences. Bulk tissue impedance decreased following IRE treatment (Fig. 4b–c). Statistical analysis demonstrated the null hypothesis was valid for the 1P ($p = 0.383$), 5P ($p = 0.675$), 10P ($p = 0.072$), and 20P ($p = 0.099$) groups. For the remaining groups of 40P and 80P, the null hypothesis was rejected though R^2 to the shared curve fits remained 0.989 ($p = 0.019$) and 0.976 ($p = 0.003$), respectively.

C. High-Frequency Impedance Measurements are Less Susceptible to EP

Increase in temperature during PEF treatment is visualized in Fig. 5a–c, g. The maximum ΔT occurred at the end of treatment, measuring ≈ 20.9 °C (Fig. 5g).

Inter-burst EIS and H-FIRE waveforms were interlaced (Fig. 5d) to quantify the change in inter-burst impedance throughout treatment. Due to equipment limitations, only inter-burst EIS waveforms were recorded. Fig. 5e shows a subset of data indicating change in electric current from baseline to the end of treatment. $\Delta\theta$ analysis was conducted using the calculated real part of the impedance (Fig. 5f). As seen in Fig. 5g, if impedance changes are entirely attributed to that of Joule heating, a $\Delta\theta$ exceeding 100°C is calculated at 1.81 kHz. The $\Delta\theta$ analysis demonstrated a convergence of $\Delta\theta$ to the true ΔT at higher frequencies, indicative of reduced EP effects at these frequencies. The maximum calculated $\Delta\theta$ at 1.81 kHz, 17.5 kHz, 181 kHz, 1.23 MHz, and 2.99 MHz was 142.9 °C, 81.3 °C, 34.3 °C, 21.7 °C, and 17.4 °C, respectively. Lastly, $\Delta\theta_{Max}$, the maximum $\Delta\theta$ in the $\Delta\theta$ profile, is plotted for all frequencies as quantified using both the real part of the impedance and the magnitude of the impedance and is shown in Fig. 5h.

Here it is noted that following ~50 H-FIRE bursts, the slope of the $\Delta\theta$ profiles across all frequencies is similar. In the circuit model analogy (Fig. 1b), if the applied voltage drastically reduces the membrane resistance R_m, the inter-burst impedance is a function of $R_e||R_i$, EP effects have subsided and therefore tissue impedance changes are likely primarily caused by Joule Heating effects.

IV. Discussion

A. Broadband Impedance Spectroscopy with Rapid EIS

The goal for this section of the study was to demonstrate rapid EIS is achievable using pulsing parameters currently applied in EBTs. An inter-burst EIS waveform consisting of a high frequency signal 1-50-1-50 μs (energized-time 164 μs) appended to a low frequency signal 250-10-250-10 μs (energized-time 1 ms) was identified to reliably capture impedance with a frequency range spanning 1.8 kHz – 4.9 MHz at 216 discrete frequencies. Nonlinear regression demonstrated the real part of the impedance did not deviate significantly from that of a calibrated commercial potentiostat within a frequency range 1.8 kHz – 1.0 MHz, (Fig. 3). It should be noted, the imaginary part of the impedance Z_{imag} started to deviate from potentiostat measurements at higher frequencies. Discrepancies between the two measurements can possibly be attributed to cable parasitics at higher frequencies. A compounding effect may be related to a reduction in the signal-to-noise ratio at high frequencies; this might be address-able by non-uniform sampling of the voltage and current signal to favor high sampling near the rising and falling edges of the pulse and decreased sampling at low frequency components [46]. Despite these differences, we demonstrate R^2 indicative of good agreement (Fig. 3). Calibration to remove hardware parasitics was not performed; variants of this configuration are encouraged to perform such calibrations, as this can play a role in measured impedance. It should further be noted, these waveforms were tested at relatively high voltages (~15 V); commercial potentiostats restrict the maximum induced potential, in this case to 3 V, to avoid stimulation of the testing load. As tissue EP occurs on the order of 100's of V/cm, the application of 15 V (~21 V/cm) was considered to remain sub-EP and allowed for high signal-power in V(f) & I(f).

Two factors limiting impedance acquisition at high frequencies include the minimum pulse-width tested (1 μs) and the threshold for peak acquisition (2% of $|V_{FFT}|$). The pulse-width is readily modifiable, though the 1 μs restriction was imposed as this is on the lower-end of pulses used *in vitro*, *ex vivo*, and *in vivo* with H-FIRE therapy [37], [38]. Nonetheless, the proposed charge-balanced bipolar chirp signal enables impedance capture with a frequency band comparable to current efforts of bioimpedance characterization; Ivorra et al. from 1 – 400 kHz [15], García-Sánchez et al. from 5 kHz – 1.313 MHz [32], Zhao et al. from 1 Hz – 1 MHz [43], and others [14], [47]–[49]. It should be noted, the parameters for inter-burst EIS and H-FIRE were selected as the pulse widths 1 μs and 2 μs are currently employed with H-FIRE. The use of these pulse widths facilitates integration of the proposed inter-burst EIS waveform to existing nsPEFs, IRE/ECT, and H-FIRE pulse generators. Parameters of the rectangular bipolar chirp signal are readily modifiable to achieve a desired bandwidth and frequency content. Waveforms like the multisine burst are exceptional for these applications, though emphasis on bipolar pulses is desired such that future implementation into standalone units is achieved, as recently investigated [50]. In that study, authors demonstrate a device capable of interlacing HV and LV pulses, though pulses with fixed pulse widths were investigated which can limit the frequency bandwidth. Further investigations directed towards optimizing signal duration, sampling, and frequency content are warranted, though not a focus of this study. Namely, rapid EIS measurements of high frequency signals will benefit from use of sharp rise-times, short-pulse widths, and nonuniform sampling [46].

Though not the focus of this study, the use of a charge balanced bipolar chirp waveform can minimize the excitation of cardiomyocytes, skeletal muscle fibers, and nerve fibers to further extend application of this waveform [51].

B. Comments on the Fourier Analysis

Fourier analysis with the FFT algorithm is indeed limited to systems that are approximately linear, time-invariant. Previous reports of impedance recovery (membrane recovery) following EP indicate a ”slow” and ”fast” impedance recovery time constant of 1.41 s and 155.3 ms, respectively, for an applied electric field 1,200 V/cm [32]. Inter-burst EIS in this study was conducted using a ~10 ms bipolar chirp signal. Therefore, it is recommended to minimize the chirp duration so as to minimize the effects of time-variance associated with the cell membrane recovery dynamics. In addition, the amplitude of this signal should be restricted to avoid inducing tissue EP and exclude capture of significant nonlinearities due to EP.

C. High-Frequency Impedance Measurements can Delineate Thermal Effect from EP

As low-frequency currents are mostly restricted to the extracellular domain prior to EP, membrane permeabilization throughout PEF treatment greatly influences impedance changes. High-frequency impedance measurements, corresponding to currents which short the membrane reactance and penetrate the cell membrane, are therefore less susceptible to EP-effects. We hypothesized high-frequency impedance measurements can serve as a reference to delineate impedance changes due to thermal effects throughout PEF treatment.

The relationship between the proposed $\Delta\theta$ analysis and ΔT was explored using a prototype device which enabled interlacing of inter-burst impedance measurements and H-FIRE (Fig. 5d). Our results revealed, in our flat-plate configuration, impedance measurements above ~0.9 MHz were not prone to EP effects (Fig. 5g–h), demonstrating a delineation between EP and thermal effects in measured impedance at higher frequencies. Calculated $\Delta\theta$ at this frequency closely approximate the true ΔT when assuming a linear relationship between the measured impedance and calculated temperature rise. Here, a temperature coefficient α = 3.0 %/°C was used for analysis [44].

A comparison between FLIR measured ΔT and $\Delta\theta$ at frequencies 1.23 MHz and 2.99 MHz demonstrates good agreement, though the maximum $\Delta\theta$ at 2.99 MHz is slightly lower than the true maximum ΔT. This could be caused by multiple factors, including the phenomenon of a distributed time constant/relaxation time found in complex biological tissues [52]. As such, it may be that rather than a single frequency being used to describe this thermal analysis, a range of frequencies may be suitable for approximating temperature rise and/or thermal contributions with an acceptable error in approximation. Fig. 5e showcases a very critical phenomenon: above ~900 kHz, the convergence of $\Delta\theta$ to ΔT indicates this frequency range suitable to approximating the true ΔT using only electrical impedance measurements and literature reported temperature coefficient of conductivity. As it is known high-frequency currents short the cell membrane reactance, the identification of a ”thermal frequency range” can be conducted *a priori* and this frequency range utilized in subsequent treatments. Lastly, the slight under-approximation of $\Delta\theta$ at 2.99 MHz (Fig. 5e) could be due

to a dependence of α on frequency or in general, the use of an average α value. While a change in α results in a change in $\Delta\theta$ values, these changes are much more pronounced at lower frequencies while higher-frequencies are less sensitive to this. Nonetheless, the determination of α or range of α should be further explored.

Upon translation to more clinically relevant electrode configurations, i.e. a two-needle configuration, the high-frequency impedance measurements are bulk impedance measurements. Therefore an approximation of ΔT may not be easily attained, though it may be possible to describe a thermal damage index to approximate the anticipated thermal damage from the real-time high-frequency impedance measurements. Furthermore, as demonstrated in Fig. 1c, once a ”thermal frequency” is identified, the effects of Joule heating may be subtracted from the impedance spectrum, thereby providing a thermal adjustment which isolates impedance changes due to EP. Isolation of impedance change due strictly to EP (by means of rapid EIS) can therefore serve as an *in situ* technique to quantify patient-specific and tissue-specific tissue conductivity and the changes in conductivity due to EP. This data can then serve to inform a patient-specific treatment planning algorithm, employed immediately following treatment to approximate the expected of ablation. For instance, once treatment is completed, the recorded impedance can be used to back out the extent of tissue EP, defined as σ_f/σ_0 [16], [53], as well as the patient specific σ_0. Construction of patient-specific treatment planning algorithms are typically based on *a priori* characterization of sigmoid conductivity curves [54]–[56]. This methodology is of particular interest as conductivity changes can be quantified on a patient-to-patient basis and take into account conductivity effects due to edema, tissue necrosis, tumor calcification, etc.

A tissue level impedance analysis for which thermal effects are compensated would provide further insight towards the effects of EP. Previously, compensation for thermal effects on measured impedance is quantified using:

$$\sigma(E,T) = \sigma(E) \cdot (1 + \alpha \cdot \Delta T) \tag{5}$$

where $\sigma(E)$ is the conductivity change due to EP [18], [57]. To quantify conductivity changes due to temperature, temperature recordings must be implemented. In the proposed methodology, it is possible to propose the identification and isolation of thermal effects on measured impedance change without temperature measurements of external devices. As the change in conductivity $\sigma(T)$ is dependent on temperature, a high-frequency reference using the proposed method can be used to approximate ΔT, and then utilize equation (5) to remove temperature effects from the low-frequency impedance. This in effect allows for the isolation of $\sigma(E)$ and Z absent of thermal effects, which can be utilized to inform of the extent of EP and/or ablation towards the determination of an ablation endpoint.

Lastly, pulses which selectively affect intracellular structures (R_i), like nanosecond PEFs, warrant further investigations as there is a potential to selectively heat intracellular organelles. Though, as electric current similarly flows through the extracellular current path, it is suspected this methodology would still apply.

Assumption/limitations: As demonstrated by Pliquett et al. [58], heat dissipation for a needle electrode configuration is significant, though also highly dependent on the location under monitoring. By utilizing a flat-plate electrode configuration as well as a relatively large tissue body, our assumption is that there is minimal heat dissipation between pulse cessation and the sampling period of the FLIR (33.33 ms). Numerical simulations (not included here) were performed to verify this assumption and results indicated 2.82% heat dissipation from the end of PEF to the thermal camera sampling period ($T_{s,}$ FLIR) 33.33 ms. As the inter-burst EIS was conducted ~500 ms following H-FIRE burst, $T_{s,}$ FLIR is of high enough resolution to capture these heat dissipation effects.

D. Potential Applications of rapid inter-burst EIS

Extrapolating these findings to clinical EP, it is possible to describe an EBT where inter-burst EIS waveforms are interlaced with H-FIRE, thereby enabling continuous high-bandwidth inter-burst EIS throughout treatment. This combination of pulsing can be used to continually monitor the absolute change in tissue impedance with a high-frequency reference to subtract thermal effects as mentioned previously. Within this treatment modality, recovery dynamics of measured inter-burst impedance can be further explored.

Potentially, a clinical endpoint dictating tumor IRE ablation may be defined using a metric such as the disintegration index, which has been extensively investigated previously for food technologies [59], [60]. A proposed approach is based on circuit model shown in Fig. 1b., where the complete reduction of the variable membrane resistance leads to a state in which the tissue impedance is approximately $R_e||R_i$. By continuously monitoring the magnitude of R_e and it's convergence to $R_e||R_i$, using the inter-burst EIS waveform, one may dictate a pulse cessation endpoint when this value is reached. In parallel to the disintegration index, this approach monitors the convergence of the σ_i (intact) to σ_d (destroyed), where σ_i represents the "low-frequency impedance measurement" and the σ_d is a "high-frequency reference" as this reference is less susceptible to EP effects. Strengths of the proposed approach include the ability to determine patient-specific clinical endpoints. The state of the tissue, for instance the extent of tissue necrosis, edema in the vicinity of treatment, calcification of tumor tissue, etc., would be accounted for in the determination of the clinical endpoint as this endpoint is marked by the convergence of intact $Z_{\text{low-frequency}}$ to $Z_{\text{high-frequency}}$.

Previously, Neal et al. described a combination low-frequency (kHz) and high-frequency (MHz) impedance measurement to approximate the nonelectroporated and fully electroporated tissue conductivity to inform treatment planning algorithms [18]. This analysis can be realized by constructing a pre-treatment impedance spectrum with the proposed inter-burst EIS waveform. The identified "thermal frequency range" of the thermal delineation analysis likely represents the frequencies which approximates the fully electroporated tissue conductivity. The rationale being that electric currents at these frequencies fully penetrate the cell membrane prior to EP, resulting in impedance as a function of $R_e||R_i$. Therefore, patient-specific sigmoid conductivity curves approximating σ_0 from the low-frequency impedance measurement and σ_f from the high-frequency impedance measurement may be determined *in situ* for various tissues including tumors, healthy tissue,

and diseased tissue. This approach also accounts for patient-to-patient variability as well as local tissue-to-tissue variability, for example pockets of necrotic tissue/necrotic cores within tumors.

Furthermore, it may be possible to monitor differences in cell death mechanisms accompanying EBTs. Contrary to cell lysis, apoptosis and necroptosis are slower in resolving cell death. Therefore, exchange in intra- and extra-cellular content during these processes may be determined with inter-burst EIS waveforms, where cell lysis may resolve in immediate impedance change with no recovery. In clinic, these impedance measurements may indicate the type of cell death experienced with EBTs. Furthermore, it's been previously proposed electric current measurements can be used to predict an accompanying immune response following IRE therapy, inter-burst EIS may be used to further investigate this phenomenon [61].

V. Conclusion

Tissue impedance changes during EBTs are indicative of treatment progression. Therefore, we utilize rapid EIS for monitoring tissue impedance changes during EBTs in real-time. The proposed charge balanced, bipolar rectangular chirp (1-50-1-50 + 250-10-250-10 μs), aimed towards monitoring inter-burst impedance, demonstrated impedance capture between 1.8 kHz - 4.93 MHz at 216 data points discrete frequencies. This waveform demonstrated good agreement against a commercial potentiostat for measuring tissue impedance change throughout IRE treatment in potato tissue. For the first time, we show impedance analysis at high-frequencies can delineate thermal effects from EP effects in measured impedance. Applications of this approach include patient-specific monitoring of ablation outcome. Further development of rapid EIS as an intraoperative tool for monitoring treatment progression is warranted.

Acknowledgment

This work was in part funded by the National Institutes of Health/National Cancer Institute P01CA207206, R01CA213423, and SBIR Phase 1 R43CA233158. This work was also funded in part by the Virginia Biosciences Health Research Corporation "The Catalyst." and the Center for Innovative Technology CRCF SBIR 19-002-LS. M.F. Lorenzo was further funded by the Cunningham Doctoral Fellowship at Virginia Tech. The authors would like to further acknowledge support the Institute of Critical Technology and Sciences (ICTAS) and its Center for Engineered Health (CEH) at Virginia Tech. Finally, all authors have patents related to the subject area. In addition, C.B. Arena and R.V. Davalos are founders of a startup company related to electroporation-based therapies.

References

[1]. Habash RW et al., "Thermal therapy, part 1: an introduction to thermal therapy," Critical Reviews™ in Biomedical Engineering, vol. 34, no. 6, 2006.

[2]. Narayanan G et al., "Vessel patency post irreversible electroporation," Cardiovascular and interventional radiology, vol. 37, no. 6, pp. 1523–1529, 2014. [PubMed: 25212418]

[3]. Li W et al., "The effects of irreversible electroporation (ire) on nerves," PloS one, vol. 6, no. 4, 2011.

[4]. Geboers B et al., "High-voltage electrical pulses in oncology: Irreversible electroporation, electrochemotherapy, gene electrotransfer, electrofusion, and electroimmunotherapy," Radiology, p. 192190, 2020.

[5]. Mali B et al., “Antitumor effectiveness of electrochemotherapy: a systematic review and meta-analysis,” european Journal of surgical Oncology (eJsO), vol. 39, no. 1, pp. 4–16, 2013. [PubMed: 22980492]

[6]. Cemazar M and Sersa G, “Recent advances in electrochemotherapy,” Bioelectricity, vol. 1, no. 4, pp. 204–213, 2019.

[7]. Davalos RV, Mir L, and Rubinsky B, “Tissue ablation with irreversible electroporation,” Annals of biomedical engineering, vol. 33, no. 2, p. 223, 2005. [PubMed: 15771276]

[8]. Martin RC et al., “Treatment of 200 locally advanced (stage iii) pancreatic adenocarcinoma patients with irreversible electroporation: safety and efficacy,” Annals of surgery, vol. 262, no. 3, pp. 486–494, 2015. [PubMed: 26258317]

[9]. Aycock KN and Davalos RV, “Irreversible electroporation: Background, theory, and review of recent developments in clinical oncology,” Bioelectricity, vol. 1, no. 4, pp. 214–234, 2019.

[10]. van den Bos W et al., “Mri and contrast-enhanced ultrasound imaging for evaluation of focal irreversible electroporation treatment: results from a phase i-ii study in patients undergoing ire followed by radical prostatectomy,” European radiology, vol. 26, no. 7, pp. 2252–2260, 2016. [PubMed: 26449559]

[11]. Felker ER et al., “Irreversible electroporation: defining the mri appearance of the ablation zone with histopathologic correlation in a porcine liver model,” American Journal of Roentgenology, vol. 208, no. 5, pp. 1141–1146, 2017. [PubMed: 28177652]

[12]. de Senneville BD et al., “Mr thermometry for monitoring tumor ablation,” European radiology, vol. 17, no. 9, pp. 2401–2410, 2007. [PubMed: 17701184]

[13]. Voyer D et al., “Dynamical modeling of tissue electroporation,” Bioelectrochemistry, vol. 119, pp. 98–110, 2018. [PubMed: 28934689]

[14]. Castellví Q, Mercadal B, and Ivorra A, “Assessment of electroporation by electrical impedance methods,” in Handbook of electroporation. Springer-Verlag, 2016, pp. 671–690.

[15]. Ivorra A and Rubinsky B, “In vivo electrical impedance measurements during and after electroporation of rat liver,” Bioelectrochemistry, vol. 70, no. 2, pp. 287–295, 2007. [PubMed: 17140860]

[16]. Bhonsle S et al., “Characterization of nonlinearity and dispersion in tissue impedance during high-frequency electroporation,” IEEE Transactions on Biomedical Engineering, vol. 65, no. 10, pp. 2190–2201, 2017. [PubMed: 29989955]

[17]. Zhao Y et al., “Characterization of conductivity changes during high-frequency irreversible electroporation for treatment planning,” IEEE Transactions on Biomedical Engineering, vol. 65, no. 8, pp. 1810–1819, 2017. [PubMed: 29989932]

[18]. Neal II RE et al., “Experimental characterization and numerical modeling of tissue electrical conductivity during pulsed electric fields for irreversible electroporation treatment planning,” IEEE Transactions on Biomedical Engineering, vol. 59, no. 4, pp. 1076–1085, 2012. [PubMed: 22231669]

[19]. Davalos RV et al., “Electrical impedance tomography for imaging tissue electroporation,” IEEE Transactions on Biomedical Engineering, vol. 51, no. 5, pp. 761–767, 2004. [PubMed: 15132502]

[20]. Granot Y et al., “In vivo imaging of irreversible electroporation by means of electrical impedance tomography,” Physics in Medicine & Biology, vol. 54, no. 16, p. 4927, 2009. [PubMed: 19641242]

[21]. Bonakdar M et al., “The feasibility of a smart surgical probe for verification of ire treatments using electrical impedance spectroscopy,” IEEE Transactions on Biomedical Engineering, vol. 62, no. 11, pp. 2674–2684, 2015. [PubMed: 26057529]

[22]. Kranjc M et al., “Predicting irreversible electroporation-induced tissue damage by means of magnetic resonance electrical impedance tomography,” Scientific reports, vol. 7, no. 1, pp. 1–10, 2017. [PubMed: 28127051]

[23]. Pliquett U, “Biophysics and metrology of electroporation in tissues,” in Handbook of Electroporation. Springer International Publishing, 2016, pp. 1–33.

[24]. Sanchez B et al., “Optimal multisine excitation design for broadband electrical impedance spectroscopy,” Measurement Science and Technology, vol. 22, no. 11, p. 115601, 2011.

[25]. Min M et al., “Broadband excitation for short-time impedance spectroscopy,” Physiological measurement, vol. 29, no. 6, p. S185, 2008. [PubMed: 18544807]

[26]. Gawad S et al., “Impedance spectroscopy using maximum length sequences: Application to single cell analysis,” Review of Scientific Instruments, vol. 78, no. 5, p. 054301, 2007.

[27]. Min M et al., “Comparison of rectangular wave excitations in broad band impedance spectroscopy for microfluidic applications,” in World Congress on Medical Physics and Biomedical Engineering, September 7–12, 2009, Munich, Germany. Springer, 2009, pp. 85–88.

[28]. Creason SC, Hayes JW, and Smith DE, “Fourier transform faradaic admittance measurements iii. comparison of measurement efficiency for various test signal waveforms,” Journal of Electroanalytical chemistry and interfacial electrochemistry, vol. 47, no. 1, pp. 9–46, 1973.

[29]. Pliquett UF and Schoenbach KH, “Changes in electrical impedance of biological matter due to the application of ultrashort high voltage pulses,” IEEE Transactions on Dielectrics and Electrical Insulation, vol. 16, no. 5, pp. 1273–1279, 2009.

[30]. Pliquett U, Langer R, and Weaver JC, “Changes in the passive electrical properties of human stratum corneum due to electroporation,” Biochimica et Biophysica Acta (BBA)-Biomembranes, vol. 1239, no. 2, pp. 111–121, 1995. [PubMed: 7488616]

[31]. Ivorra A et al., “In vivo electrical conductivity measurements during and after tumor electroporation: conductivity changes reflect the treatment outcome,” Physics in Medicine & Biology, vol. 54, no. 19, p. 5949, 2009. [PubMed: 19759406]

[32]. García-Sánchez T et al., “Interpulse multifrequency electrical impedance measurements during electroporation of adherent differentiated myotubes,” Bioelectrochemistry, vol. 105, pp. 123–135, 2015. [PubMed: 26123676]

[33]. García-Sánchez T, Bragós R, and Mir LM, “In vitro analysis of various cell lines responses to electroporative electric pulses by means of electrical impedance spectroscopy,” Biosensors and Bioelectronics, vol. 117, pp. 207–216, 2018. [PubMed: 29906768]

[34]. Bürgel SC et al., “On-chip electroporation and impedance spectroscopy of single-cells,” Sensors and Actuators B: Chemical, vol. 210, pp. 82–90, 2015.

[35]. Sanchez B et al., “Basics of broadband impedance spectroscopy measurements using periodic excitations,” Measurement Science and Technology, vol. 23, no. 10, p. 105501, 2012.

[36]. Beebe SJ et al., “Nanosecond pulsed electric field (nspef) effects on cells and tissues: apoptosis induction and tumor growth inhibition,” IEEE Transactions on plasma science, vol. 30, no. 1, pp. 286–292, 2002.

[37]. Arena CB et al., “High-frequency irreversible electroporation (h-fire) for non-thermal ablation without muscle contraction,” Biomedical engineering online, vol. 10, no. 1, p. 102, 2011. [PubMed: 22104372]

[38]. O’Brien TJ et al., “Experimental high-frequency irreversible electroporation using a single-needle delivery approach for nonthermal pancreatic ablation in vivo,” Journal of Vascular and Interventional Radiology, vol. 30, no. 6, pp. 854–862, 2019. [PubMed: 31126597]

[39]. Vižintin A et al., “Effect of interphase and interpulse delay in high-frequency irreversible electroporation pulses on cell survival, membrane permeabilization and electrode material release,” Bioelectrochemistry, p. 107523, 2020. [PubMed: 32272337]

[40]. Lorenzo MF et al., “Temporal characterization of blood–brain barrier disruption with high-frequency electroporation,” Cancers, vol. 11, no. 12, p. 1850, 2019.

[41]. Sersa G et al., “Electrochemotherapy in treatment of tumours,” European Journal of Surgical Oncology (EJSO), vol. 34, no. 2, pp. 232–240, 2008. [PubMed: 17614247]

[42]. Sharabi S et al., “The effects of point-source electroporation on the blood-brain barrier and brain vasculature in rats: An mri and histology study,” Bioelectrochemistry, p. 107521, 2020. [PubMed: 32251984]

[43]. Zhao Y et al., “Ablation outcome of irreversible electroporation on potato monitored by impedance spectrum under multi-electrode system,” Biomedical engineering online, vol. 17, no. 1, p. 126, 2018. [PubMed: 30236121]

[44]. Boussetta N et al., ““cold” electroporation in potato tissue induced by pulsed electric field,” Journal of food engineering, vol. 115, no. 2, pp. 232–236, 2013.

[45]. Redondo L, Zahyka M, and Kandratsyeu A, “Solid-state generation of high-frequency burst of bipolar pulses for medical applications,” IEEE Transactions on Plasma Science, vol. 47, no. 8, pp. 4091–4095, 2019.

[46]. Pliquett U et al., “Fast broad bandwidth bioimpedance measurement-the use of square wave excitation and non-uniform sampling,” in 2012 13th Biennial Baltic Electronics Conference. IEEE, 2012, pp. 279–282.

[47]. Stolwijk JA et al., “Impedance analysis of adherent cells after in situ electroporation: non-invasive monitoring during intracellular manipulations,” Biosensors and Bioelectronics, vol. 26, no. 12, pp. 4720–4727, 2011. [PubMed: 21684144]

[48]. Pasqualotto E et al., “Monitoring electropermeabilization of adherent mammalian cells through electrochemical impedance spectroscopy,” Procedia Chemistry, vol. 6, pp. 79–88, 2012.

[49]. Dean D et al., “Electrical impedance spectroscopy study of biological tissues,” Journal of electrostatics, vol. 66, no. 3–4, pp. 165–177, 2008. [PubMed: 19255614]

[50]. López-Alonso B et al., “Real-time impedance monitoring during electroporation processes in vegetal tissue using a high-performance generator,” Sensors, vol. 20, no. 11, p. 3158, 2020.

[51]. Reilly JP, Freeman VT, and Larkin WD, “Sensory effects of transient electrical stimulation-evaluation with a neuroelectric model,” IEEE transactions on biomedical engineering, no. 12, pp. 1001–1011, 1985. [PubMed: 4077078]

[52]. Pethig R and Kell DB, “The passive electrical properties of biological systems: their significance in physiology, biophysics and biotechnology,” Physics in Medicine & Biology, vol. 32, no. 8, p. 933, 1987. [PubMed: 3306721]

[53]. Ivorra A, Mir L, and Rubinsky B, “Electric field redistribution due to conductivity changes during tissue electroporation: experiments with a simple vegetal model,” in World Congress on Medical Physics and Biomedical Engineering, September 7–12, 2009, Munich, Germany. Springer, 2009, pp. 59–62.

[54]. Sel D et al., “Sequential finite element model of tissue electropermeabilization,” IEEE Transactions on Biomedical Engineering, vol. 52, no. 5, pp. 816–827, 2005. [PubMed: 15887531]

[55]. Beitel-White N et al., “Multi-tissue analysis on the impact of electroporation on electrical and thermal properties,” IEEE Transactions on Biomedical Engineering, 2020.

[56]. Corovic S et al., “Modeling of electric field distribution in tissues during electroporation,” Biomedical engineering online, vol. 12, no. 1, p. 16, 2013. [PubMed: 23433433]

[57]. Zhao Y et al., “Development of a multi-pulse conductivity model for liver tissue treated with pulsed electric fields,” Frontiers in Bioengineering and Biotechnology, vol. 8, p. 396, 2020. [PubMed: 32509742]

[58]. Pliquett U, “Joule heating during solid tissue electroporation,” Medical and Biological Engineering and Computing, vol. 41, no. 2, pp. 215–219, 2003. [PubMed: 12691444]

[59]. Knorr D and Angersbach A, “Impact of high-intensity electric field pulses on plant membrane permeabilization,” Trends in Food Science & Technology, vol. 9, no. 5, pp. 185–191, 1998.

[60]. Lebovka N, Bazhal M, and Vorobiev E, “Estimation of characteristic damage time of food materials in pulsed-electric fields,” Journal of Food Engineering, vol. 54, no. 4, pp. 337–346, 2002.

[61]. Beitel-White N et al., “Real-time prediction of patient immune cell modulation during irreversible electroporation therapy,” Scientific reports, vol. 9, no. 1, pp. 1–8, 2019. [PubMed: 30626917]

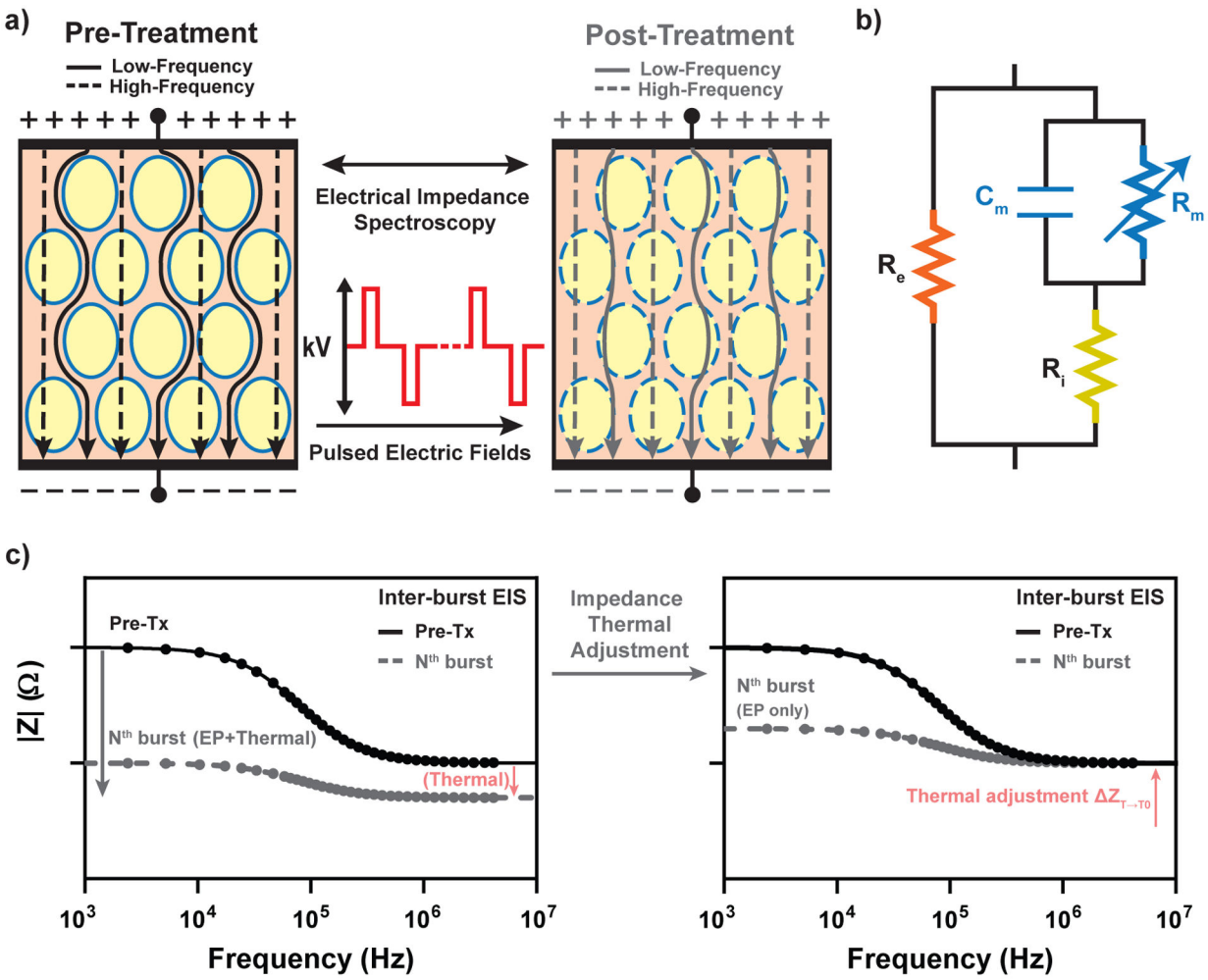

Fig. 1.

Depiction of (a) inter-burst EIS prior to and after cell electroporation. High-voltage PEFs compromise the cell membrane, allowing current to flow through the cell. This behavior can be described using a (b) circuit model representation [13], resulting in characteristic impedance spectra like that in (c). As high-frequency currents are less susceptible to EP effects, we hypothesize these impedance changes to delineate EP effects from that of thermal effects (c).

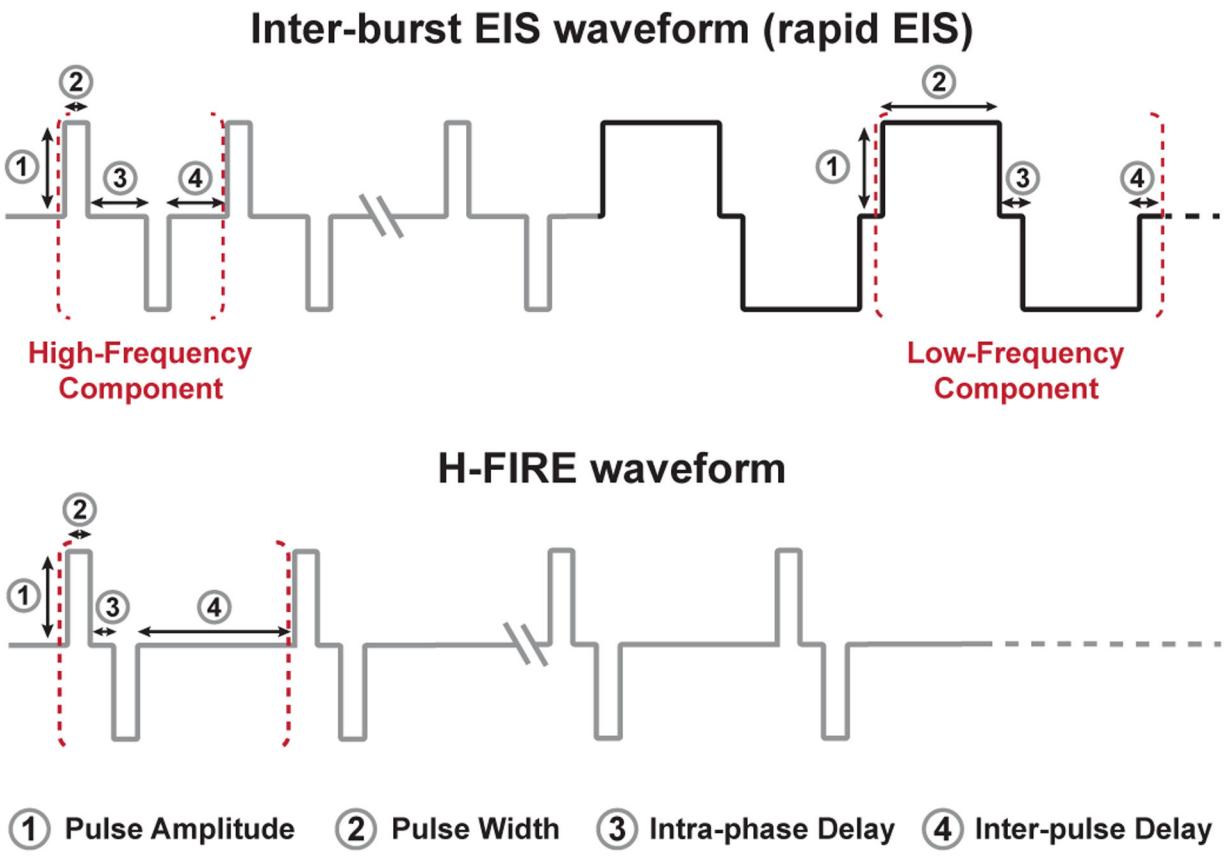

Fig. 2.

Schematic of inter-burst EIS and H-FIRE waveforms. The nomenclature for the burst is: positive phase – intra-phase delay – negative phase – inter-pulse delay μs. This represents a single set of bipolar pulses and is repeated for a desired energized-time.

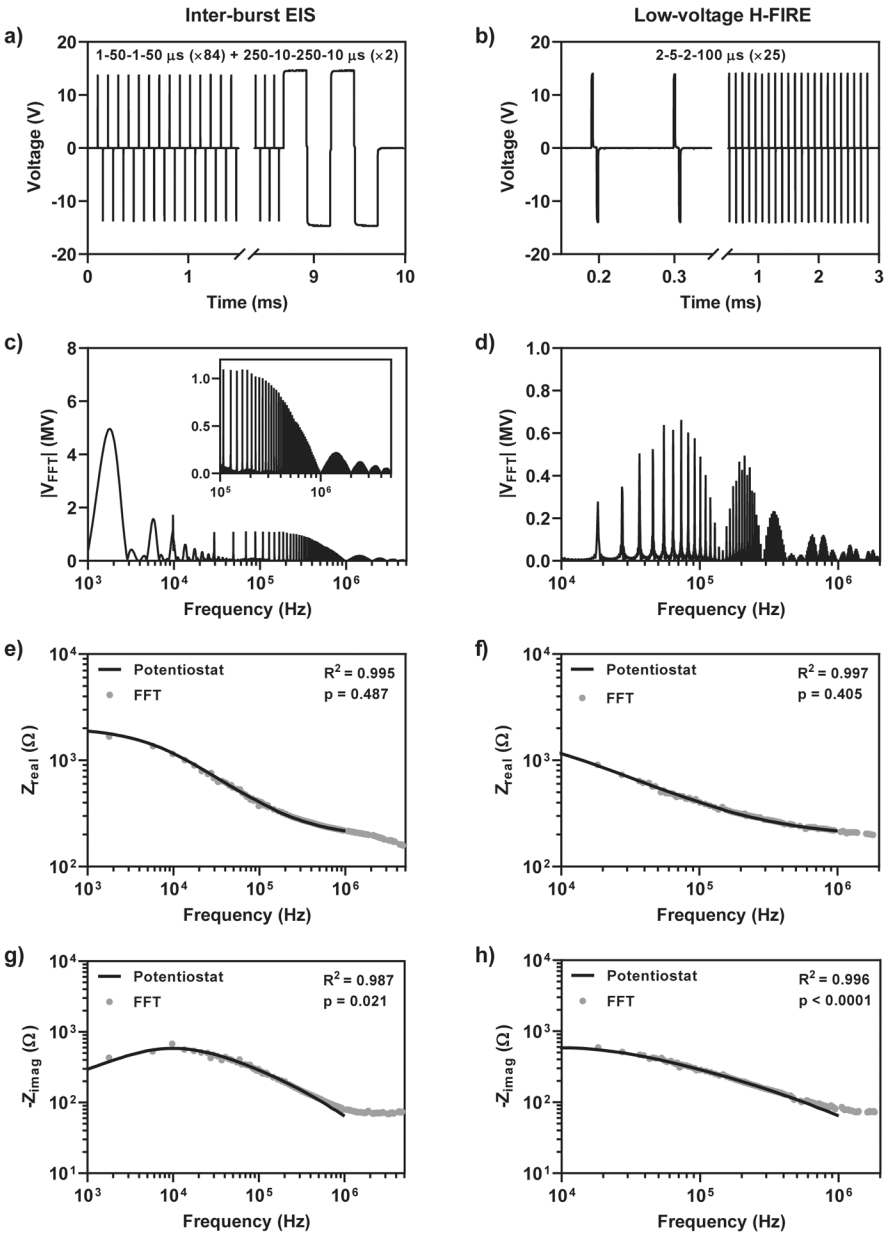

Fig. 3.

Validation of (a) inter-burst EIS waveform 1-50-1-50 μs (×84) + 250-10-250-10 μs (×2) and (b) H-FIRE 2-5-2-100 μs (×25) impedance measurements in potato tissue. Impedance data were extracted from each high-power peak in $|V_{FFT}|$ and are shown in (c) and (d). The real and imaginary impedance are shown in (e)-(h). Nonlinear regression was conducted and a global fit determined between the potentiostat and inter-burst/H-FIRE data.

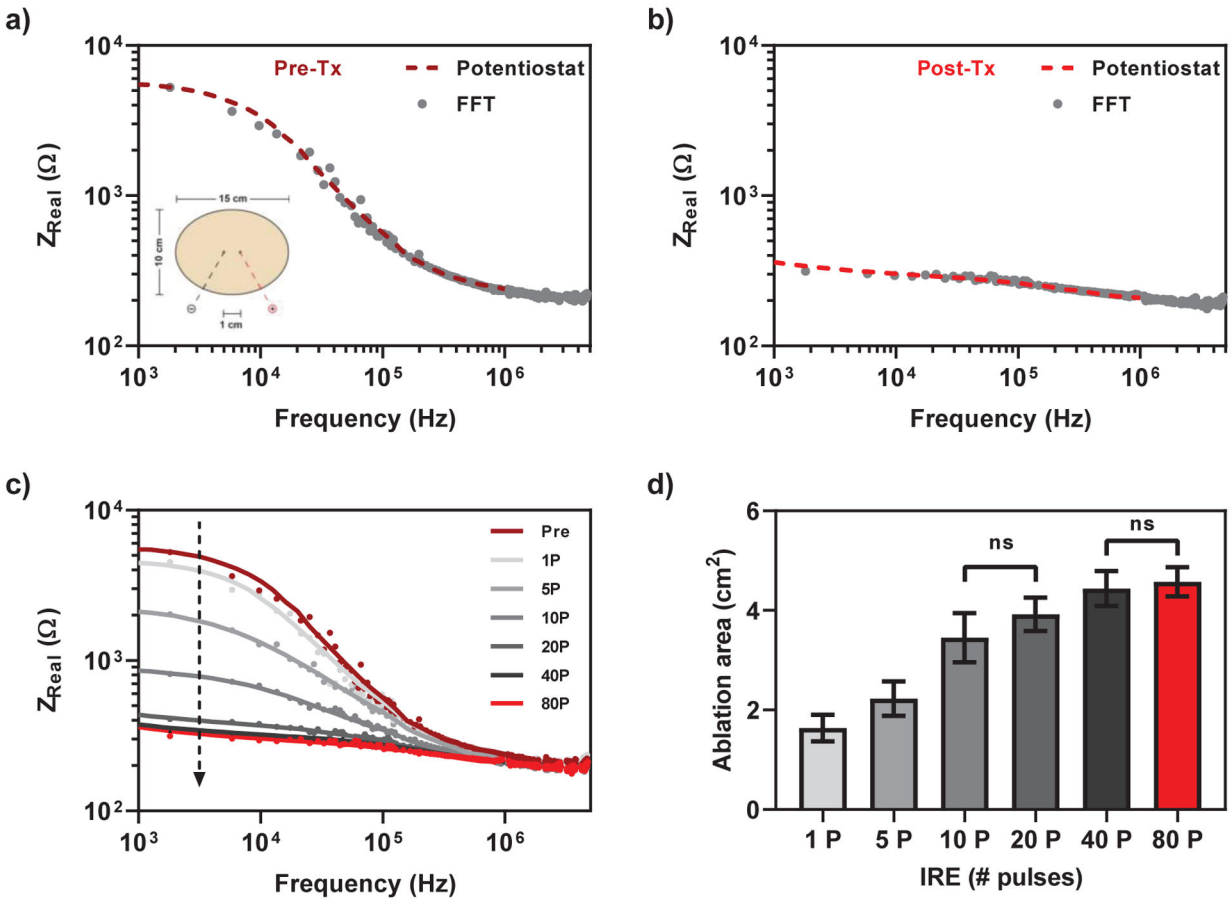

Fig. 4. Rapid inter-burst EIS to monitor extent of electroporation during IRE treatment.

Inter-burst EIS waveform was used to measure bulk potato impedance prior to (a) and following (b)-(c) 1, 5, 10, 20, 40, and 80 IRE pulses (1000 V, 100 μs energized time). In all cases, except for those labeled on the graph, (d) ablation areas were statistically different from one another ($p < 0.05$).

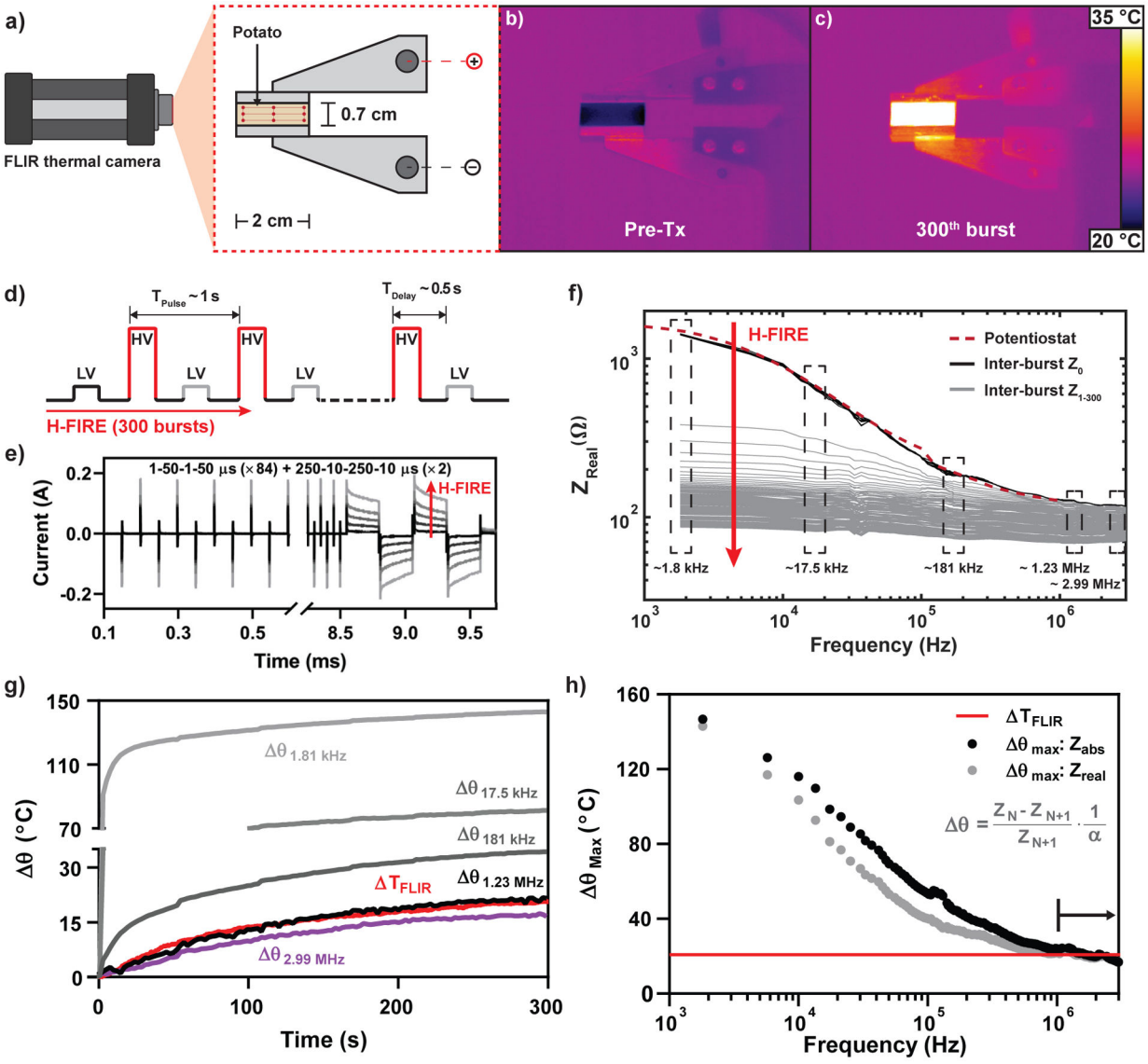

Fig. 5. High-frequency impedance measurements to delineate thermal and EP effects.

A FLIR thermal camera (a)-(c) was used to record temperature throughout H-FIRE (300 bursts, 1400 V). A prototype board was constructed to allow for (d)-(f) interlacing of low-voltage inter-burst EIS measurements throughout H-FIRE therapy. (e) demonstrates inter-burst electric current measurements throughout treatment. 5 baseline impedance spectra were measured and (f) inter-burst impedance recorded at 0.5 Hz. A $\Delta\theta$ analysis was conducted for the impedance changes (real part of the impedance) throughout H-FIRE to investigate a convergence of $\Delta\theta$ to the true ΔT. Analysis of the $\Delta\theta$ demonstrates (g)-(h) low frequencies over-approximate ΔT in comparison to a high-frequency signal. (h) demonstrates the $\Delta\theta_{Max}$ for all frequencies as quantified using either the real part of the impedance or the magnitude of the impedance. Measured impedance changes at $f >$ ~0.9 MHz best approximate the measured ΔT, as these frequencies presumably minimize impedance changes from initial EP effects.

TABLE I

Monitoring extent of electroporation with Inter-burst EIS

IRE Ablation - Two-Needle Configuration			Nonlinear Regression	
Group	**Pulse # × sets**	**Ablation [cm^2]**	**p-value**	**R^2**
0	Pre-Tx	0	0.216	0.994
1	1×1	1.63 ± 0.26	0.383	0.994
2	5×1	2.23 ± 0.34	0.675	0.991
3	10×1	3.45 ± 0.49	0.072	0.998
4	10×2	3.92 ± 0.33	0.099	0.991
5	10×4	4.43 ± 0.35	0.018 *	0.989
6	10×8	4.57 ± 0.29	0.003 *	0.976

Mean ± SD;

* $p < 0.05$, indicates global curve fit is invalid